OCTOBER 1981 LRP 188/81

MHD STUDIES ON ALFVEN WAVE HEATING OF LOW-β PLASMAS

B. Balet, K. Appert and J. Vaclavik

MHD STUDIES ON ALFVEN WAVE HEATING OF LOW-β PLASMAS

B. BALET, K. APPERT AND J. VACLAVIK

Centre de recherches en physique des plasmas

Association Euratom - Confédération Suisse

Ecole Polytechnique Fédérale de Lausanne

CH - 1007 Lausanne - Switzerland

ABSTRACT

The energy absorption of rf waves at the spatial Alfvén resonance of a cylindrical plasma is investigated using ideal MHD equations. It is found that the absorbed power exhibits a resonant enhancement if a collective mode is excited. The dependence of the optimal power upon the characteristics of the plasma equilibrium, the type of the antenna-shell configuration and the type of the collective mode is established.

1. INTRODUCTION

It is widely recognized that supplementary heating, in addition to the basic ohmic heating, will be necessary to bring a tokamak reactor into the ignition regime. One of the many schemes proposed for this purpose is resonant absorption of Alfvén waves in a nonuniform plasma. It has the basic merit of using low-frequency rf fields for which high-power sources are readily available.

Up to now, two mechanisms were considered to heat plasma by means of Alfvén wave absorption. First, GROSSMANN and TATARONIS (1973) and HASEGAWA and CHEN (1974) showed that the existence of a continuous spectrum leads to the damping of a cutoff electromagnetic wave through the phase mixing. The basic theory for the rate of energy absorption using this mechanism has been given by CHEN and HASEGAWA (1974) using a simple slab-geometry. They found that the absorption rate is strongly enhanced when the nonuniformity of equilibrium is sharp and the driving frequency is close to the frequency of the weakly-damped surface mode (SEDLACEK, 1971). One of the objectives of the present paper is to show that a similar phenomenon takes place in an equilibrium with an arbitrary nonuniformity. In this case the surface mode becomes strongly damped, and consequently it may be called quasi-mode.

The other mechanism proposed is the excitation and subsequent absorption of magnetosonic cavity modes. The reflection coefficient for an incident magnetosonic wave has been calculated. These calculations have been performed assuming a slab geometry, uniform magnetic field and linear density profile (KARNEY et al., 1979; STIX, 1980).

Some other calculations (OTT et al., 1978) have been specialized to the m = 0 case, where m is the poloidal wave number.

In this paper we try to provide a unified picture of the Alfvén wave heating scheme from an ideal MHD viewpoint. We test numerically the two mechanisms proposed and point out their typical features, their relative advantages or disadvantages. Moreover, a systematic study of a cylindrically symmetric equilibrium permits us to establish where and how much energy will be deposited and what are the important parameters of Alfvén waves heating.

The paper is structured as follows. In Section 2 we present the basic equations of the ideal MHD theory and our numerical treatment. This section also includes the calculations of antennae, boundary conditions and power absorbed. In Section 3 we describe the Alfvén continuum and the physical process of resonant absorption. In Section 4 we mention some numerical details and explain the limits of our computational model. Sections 5 and 6 deal with physical results concerning the energy deposition versus equilibria, geometric parameters, antennae used and pump frequencies. Finally, we draw the main conclusions in Section 7.

2. BASIC EQUATIONS

2.1 Ideal MHD equations

Mathematically, the problem reduces to an investigation of small oscillations about an equilibrium state which are excited by an external source. If the oscillation amplitudes are small, the

linearized equation of motion can be used. Let ρ, $\tilde{p}$, $\underline{B}$ and $\underline{j}$ represent small deviations of density, pressure, magnetic field and current density form the equilibrium values ρ_0, p_0, $\underline{B}_0$, $\underline{j}_0$. The linearized equations of magnetohydrodynamics can then be written in the form :

$$\rho_0 \frac{\partial \underline{u}}{\partial t} = -\nabla \tilde{p} + \underline{j} \times \underline{B}_0 + \underline{j}_0 \times \underline{B} \quad , \tag{1}$$

$$\frac{\partial \tilde{p}}{\partial t} = \gamma p_0 \nabla \cdot \underline{u} - \underline{u} \cdot \nabla p_0 \quad , \tag{2}$$

$$\nabla \times \underline{B} = \mu_0 \underline{j} \quad , \quad \nabla \times \underline{E} = - \frac{\partial \underline{B}}{\partial t} \quad . \tag{3}$$

We assume an ideally conducting plasma, which implies the Ohm's law:

$$\underline{E} = - \underline{u} \times \underline{B}_0 \tag{4}$$

and with (3) yields :

$$\frac{\partial \underline{B}}{\partial t} = \nabla \times (\underline{u} \times \underline{B}_0) . \tag{5}$$

In this set of equations $\underline{u}$ is the plasma velocity and γ is the adiabaticity index. It is frequently not convenient to use the velocity $\underline{u}$; one rather treats the plasma displacement from an equilibrium position $\underline{\xi}$, defined by $\underline{u} = \partial \underline{\xi} / \partial t$.

Eqs.(2) and (5) can then be integrated with respect to time, and $\tilde{p}$, $\underline{B}$ and $\underline{j}$ can be expressed explicitly in terms of $\underline{\xi}$:

$$\begin{aligned} \tilde{p} &= - \gamma p_0 \nabla \cdot \underline{\xi} - \underline{\xi} \cdot \nabla p_0 \quad , \\ \underline{B} &= \nabla \times (\underline{\xi} \times \underline{B}_0) \quad , \\ \underline{j} &= \frac{1}{\mu_0} \nabla \times (\nabla \times (\underline{\xi} \times \underline{B}_0)) . \end{aligned} \tag{6}$$

Substitution of these expressions in Eq. (1) results in a second order differential equation for $\underline{\xi}$:

$$\rho_0 \frac{\partial^2 \underline{\xi}}{\partial t^2} = \nabla\left(\underline{\xi}\cdot\nabla p_0 + \gamma p_0 \nabla\cdot\underline{\xi}\right) + \frac{1}{\mu_0}\left(\nabla\times\left(\nabla\times\left(\underline{\xi}\times\underline{B_0}\right)\right)\right)\times\underline{B_0} + \frac{1}{\mu_0}\left(\nabla\times\underline{B_0}\right)\times\left(\nabla\times\left(\underline{\xi}\times\underline{B_0}\right)\right), \tag{7}$$

which is symbolized by: $\rho_0 \ddot{\underline{\xi}} = \underline{F}[\underline{\xi}]$,

where $\underline{F}$ is the ideal MHD restoring force.

2.2 Numerical treatment

We shall study a cylindrically symmetric equilibrium with an arbitrary non-uniformity and assume $\underline{\xi} = \underline{\xi}(r)\exp[i(-\omega t + m\theta + kz)]$. The one-dimensional spectral code THALIA (APPERT et al., 1975) can then be used to solve the eigenvalue problem corresponding to Eq. (7):

$$-\omega^2 \underline{\underline{B}}\cdot\underline{\xi} = \underline{\underline{A}}\cdot\underline{\xi}\ , \tag{8}$$

where $\underline{\underline{B}}$ and $\underline{\underline{A}}$ represent the mass and potential energy matrices, respectively.

There are two different ways to calculate numerically the "absorbed" power in the framework of ideal MHD. The first one is to solve Eq. (7), subject to the appropriate boundary conditions, as an initial value problem. The evolution code then solves the following system :

$$\underline{\underline{B}}\cdot\ddot{\underline{\xi}} = \underline{\underline{A}}\cdot\underline{\xi} + \underline{S}\sin(\omega_p t). \tag{9}$$

The second way of doing it is to add an artificial damping term ν to Eq. (8) and asking for the stationary state behaving as $\exp(-i\omega_p t)$. The equation to be solved then becomes :

$$-\omega_p^2 \underline{\underline{B}} \cdot \underline{\xi} - 2i\nu\omega_p \underline{\underline{B}} \cdot \underline{\xi} = \underline{\underline{A}} \cdot \underline{\xi} + \underline{s} . \qquad (10)$$

In both cases, $\underline{s}$ represents a source term which models a current in an antenna situated in the vacuum between the plasma and an outer shell. We have modeled two types of antennae: a helical antenna and the antenna used on TCA (CHEETHAM et al., 1980).

2.3 Antennae

Let us consider a plasma of radius r_p surrounded by antennae of vanishingly small thickness at radius r_a and a perfectly conducting outer shell at radius r_s (cf. Fig.1).
We assume an antenna current density $j_\theta = J_\theta \delta(r-r_a)$ with J_θ behaving as $\exp[i(m\theta + kz - \omega_p t)]$. The normalization is always chosen such that the total current per "wire" $I = 2J_\theta/k$ is equal to $r_p B_{oz}$.

a) Helical antenna

This antenna (cf. Fig. 2) assumes $j_r = 0$; from $\nabla \cdot \underline{j} = 0$ we then have :

$$j_z = -\frac{m}{k r_a} j_\theta = -\frac{m}{k r_a} J_\theta \delta(r-r_a) .$$

b) TCA antenna

This antenna (cf.Fig. 3), used on the TCA tokamak, assumes $j_z = 0$; $\nabla \cdot \underline{j} = 0$ then implies

$$j_r = \begin{cases} 0 & \text{if } r_p \le r < r_a \\ -\frac{im}{r} J_\theta & \text{if } r_a \le r \le r_s \end{cases} .$$

So we introduce the following generalized antenna formulation:

$$\begin{aligned} j_r &= -i \frac{m}{r} s J_\theta \quad \text{if } r \in III \; ; \; j_r = 0 \quad \text{if } r \in II , \\ j_\theta &= J_\theta \, \delta(r-r_a) , \\ j_z &= -(1-s) \frac{m}{k r_a} J_\theta \, \delta(r-r_a) , \end{aligned} \tag{11}$$

which reduces to the particular cases of the helical antenna (s = 0) or the TCA antenna (s = 1).

2.4 Boundary conditions and power absorbed

Eq. 7 must be supplemented by boundary conditions. For this purpose we introduce the vector potential $\underline{A}$ and look after differential equations describing A_z and B_z in vacuum. Using $\nabla \cdot \underline{B} = 0$ and $\nabla \times \underline{B} = \mu_0 \underline{j}$, it appears that B_z is the solution of the following differential equation:

$$D B_z = \mu_0 s \frac{m^2}{r^2} J_\theta \, H(r-r_a), \tag{12}$$

where the Bessel operator D is:

$$D = \frac{1}{r} \frac{d}{dr} r \frac{d}{dr} - \left(\frac{m^2}{r^2} + k^2 \right)$$

and the function H is defined by:

$H(x) = 1 \quad \text{if } x > 0$

$H(x) = 0 \quad \text{if } x < 0$.

In the same way $\nabla \times \underline{A} = \underline{B}$ and $\nabla \cdot \underline{A} = 0$ imply a differential equation for A_z:

$$D A_z = 0 \,. \tag{13}$$

Then we have the following boundary conditions:

a) At $r = r_s$ the tangential component of the electric field E_t must vanish, which implies:

$$A_z = 0 \quad , \quad \frac{\partial B_z}{\partial r} = 0 \,.$$

b) At $r = r_a$ the current defined by Eq. (11) and the assumption of no surface charge ($[E_r]_{II}^{III} = 0$) imply the following conditions:

$$[B_z]_{II}^{III} = J_\theta \mu_0 \quad , \qquad [A_z]_{II}^{III} = 0 \,,$$

$$\left[\frac{\partial B_z}{\partial r}\right]_{II}^{III} = 0 \quad , \quad \left[\frac{\partial A_z}{\partial r}\right]_{II}^{III} = \frac{m}{k r_a}(1-s) J_\theta \mu_0 \,.$$

Here the subscripts II and III refer to Fig. 1 and specify both sides of the antenna.

c) At $r = r_p$ the continuity of the tangential component of the electric field E_t together with the continuity of the total pressure yield:

$$\frac{\partial B_z}{\partial r} = -k F^{II} \xi_r \,,$$

$$A_z = B_{0\theta}^{II} \xi_r \,,$$

where $F(r) = k\, B_z(r) + \frac{m}{r} B_\theta(r)$

We can now express the absorbed power P, seen by the antenna:

$$P = \frac{1}{2} \int d^3r\, \underline{j} \cdot \underline{E}^* = i\omega_p \pi L \int_{r_a}^{r_s} \underline{j} \cdot \underline{A}^*\, r\, dr .$$

Here L is the length of the cylinder.

Using the Maxwell's equations, we obtain:

$$\frac{P}{\pi L} = i\omega_p (1-S) \frac{r_a}{k^2} J_\theta \mu_0 \left.\frac{\partial B_z^*}{\partial r}\right|_{r=r_a} - i\omega_p S\, J_\theta \mu_0 \int_{r_a}^{r_s} r\, B_z^*\, dr.$$

We have now to express the magnetic field B_z. To solve the differential equation (12) for B_z, we define three fundamental functions H,K and G:

a) H and K are solutions of the homogeneous case:

$D \cdot H = 0$ and $D \cdot K = 0$ with the boundary conditions

$K(r_s) = 1$, $K'(r_s) = 0$

$H(r_a) = 0$, $H'(r_a) = 1$

b) G is a particular solution of the inhomogeneous case

$D \cdot G = s\mu_0 \frac{m^2}{r^2} J_\theta$ with $G(r_s) = 1$, $G'(r_s) = 0$ as boundary conditions.

The field B_z is now given by:

$B_z = \alpha K + G$ if $r_a < r < r_s$

$B_z = \gamma K + \delta H$ if $r_p < r < r_a$

The boundary conditions for the magnetic field B_z give us the expression for the coefficient α, γ, and δ. The absorbed power is then given by:

$$\frac{\bar{P}}{\pi L} = \frac{i\omega_p}{K'_p}\left[(1-S)\frac{r_a}{k^2}K'_a - S\,\Phi_K\right]\left[-k\,F_p^{II}\,\xi^*_{rp}\,J_\theta\,\mu_0\right.$$

$$\left. + \frac{J_\theta^2\mu_0^2}{K_a}\left(H'_p K'_a - K'_p\right) + \frac{J_\theta\mu_0}{K_a}\left(H'_p\left(K'_a G_a - K_a G'_a\right) - G_a K'_p\right)\right]$$

$$+ i\omega_p J_\theta\left[(1-S)\frac{r_a}{k^2}G'_a - S\,\phi_G\right], \qquad (14)$$

where

$$\Phi_K = \int_{r_a}^{r_s} r\,K(r)\,dr\,, \qquad \Phi_G = \int_{r_a}^{r_s} r\,G(r)\,dr.$$

The subscripts a and p on the fundamentals signify the positions r_a and r_p where they are evaluated.

We will present results in terms of $\bar{P}$ = Rep/L representing the time-average resistive power per unit length and in terms of the "coupling factor" Q defined by: Q = Imp/Rep .

3. CONTINUOUS SPECTRUM AND RESONANT ABSORPTION

3.1 Equilibrium and the Alfvén continuum

For the sake of simplicity, the unperturbed plasma is described by an equilibrium with the following characteristics: $B_z = 1$, $j_z = j_0\ (1-r^2)^\alpha$, $\rho_o = 1.01 - (1.01 - \rho_a)\ r^\delta$ in dimensionless units where the plasma radius is unity (these units will be used also in the presentation of all results).

The free parameters j_0, α, ρ_a and δ are varied within certain range such that zero plasma pressure at the plasma boundary results in β-values of a few per cent on the axis.

The azimuthal and longitudinal wave numbers m and k of the plasma motion are input values given, physically, by the antenna structure. Toroidal geometry can be simulated by expressing the longitudinal wave number k in terms of the toroidal wave number n and the major radius R: $k = n/R$.

The Alfvén continuum is then determined by:

$$\omega_A^2 = (k + m B_\theta / r)^2 = B_\theta^2 (m + nq)^2 / r^2,$$

where q is the security factor $q = r/RB_\theta$.
Then, for every frequency in this range, there exists an "eigenmode" satisfaying Eq. (7). These eigenmodes have the character of distributions in space. They are not square integrable, but their superposition yields integrable, physically meaningful functions. We can compare the class of the Alfvén modes with an ensemble of infinitely many oscillators, continuously distributed in space and frequency.

3.2 Resonant process

Now let us choose the pump frequency ω_p within this continuum. A typical evolution of resonant absorption is shown on Fig. 4 by the spatial profile of the poloidal displacement ξ_θ at three subsequent times. The increasing concentration of energy around the resonant

layer $r_s = .5$ is evident. In the lower part of the picture the absorbed power is plotted versus time. The arrows indicate the times at which ξ_θ is shown. Most strikingly, after two pump periods $2\pi/\omega_p$ the value of $\bar{p}$ is already in the vicinity of the asymptotic value $\bar{p} = .021$. Note that in the evolution code $\bar{p}$ is not determined by Eq. (14) but by:

$$\bar{p} = \frac{1}{Lt} \int_0^t dt' \int d^3r \, \underline{j} \cdot \underline{E} \quad .$$

In Fig. 5 the spatial wave forms of $\mathrm{Re}\xi_\theta$ are shown as produced with the stationary version of the code. Three different values of the artificial damping coefficient ν have been used. The calculated absorbed powers agree within 10 % with each other and with that obtained by means of the evolution code. All the oscillations far from the resonant surface are damped in this case.

Let us now consider a particular equilibrium without any current and with a monotonic density profile: constant if $r < r_c$ and then falling down linearly to 10 % of its value on the axis (cf. Fig. 6). Such an equilibrium yields a simple Alfvèn continuum (which allows only one resonant surface for a given frequency). We impose an initial displacement of the plasma column and then let it oscillate freely. We then make a Fourier analysis of the radial displacement ξ_r at a given radius r: $\xi_r\,(r,t) = \sum A(r,\omega) e^{-i\omega t}$. Fig. 7 shows the amplitudes of $A(r,\omega)$ versus ω for three different radii r = .7, .76 and .9, for a longitudinal wave number k = 2 and an azimuthal wave number m = 1. For each radius r, a maximum of the amplitudes appears; this maximum M(r) occurs around $\omega_K = 2.27 \pm .03$ in all cases. This is an

indication of a global motion of the plasma column. We have tried to identify it as a global mode by means of the spectral code THALIA but unsuccessfully: the only way to point it out is to study its consequences. This mode, which may be called collective, can be understood as a remnant of the lowest-frequency fast mode which has disappeared in the continuum and which may reappear as a real eigenmode in either unstable situation (kink) or in equilibria with discontinuities (surface eigenmode). In the same way, the Fourier analysis at higher frequencies points out global motions corresponding to the second, third, etc. fast waves. Furthermore, we notice in Fig. 7 that the maximum of amplitudes M(r) depends on the radius r where the radial displacement ξ_r is Fourier-analysed; this maximum increases when $\omega_A(r)$ approachs ω_K : the closer the local Alfvèn frequency is to the frequency of the collective mode, the higher is the maximum M(r). This resonant behaviour with a collective mode is confirmed if we plot the absorbed power $\bar{p}$ obtained with the stationary version of the code versus the pump frequency ω for the same equilibrium (cf. Fig. 8). Indeed, the maximum of $\bar{p}$ occurs around $\omega_K = 2.29$ and indicates the presence of the collective mode.

4. LIMITS TO THE COMPUTATIONAL MODEL

The discretization in space imposes a discretization in frequency. The continuum is then approximated by a discrete spectrum in which the frequencies are related to the local Alfvén frequencies on the radial mesh. The validity conditions then require that the code should be unaware of the discreteness of the continuum as long as at least two frequencies are resonant with the pump.

Then, if $\Delta\omega$ is the ω-mesh spacing at the resonant surface, it appears that the evolution code is valid up to a time $t_{max} = 2\pi/\Delta\omega$ and the stationary code is valid if the artificial damping $\nu > \Delta\omega$. These limits are evident on the next figures where the absorbed power $\bar{p}$ is plotted versus time (Fig. 9) or versus the artificial damping ν (Fig. 10) for the same equilibrium parameters. Two pump frequencies have been chosen differing by $\Delta\omega/2$. The frequency ω_{p1} was equal to an eigenfrequency in the "continuum", the frequency ω_{p2} on the other hand lay between two eigenfrequencies: this explains the different behaviour of the curves beyond the validity limits. However, for $\nu > \Delta\omega$ or $t < t_{max} = 2\pi/\Delta\omega$ the system does not feel distinct eigenvalues and produces the same value of $\bar{p}$ for the two frequencies. For the stationary code, however, the magnitude of the artificial damping ν must be chosen sufficiently small that the results do not depend on it. The problem treated here is analogous to the case of a damped harmonic oscillator when acted on by a force with a continuous spectrum. The total energy absorbed by the oscillator does not depend on the attenuation decrement when the attenuation is weak. Thus, we calculated the "true" resonant absorption without specifying a dissipation mechanism. In conclusion, for the evolution and stationary codes, we need a good spectral and spatial representation of the continuum. The stationary version is much less time consuming than the evolution one but cannot give us the time behaviour of the displacement $\underline{\xi}$.

5. SURFACE QUASI-MODE (KINK-LIKE MODE) COUPLING

In section 3.2, the resonant behaviour of the absorbed power due to the presence of a surface mode (the lowest-frequency strongly-

damped fast mode) was pointed out. The stationary code permits us to study this phenomenon systematically by computing the altitude chart of the absorbed power $\bar{p}$ in the ωk-plane. Such a chart is shown in Fig. 11 for the m = 1 excitation and the equilibrium given by $j_0 = .6$, $\alpha = 2$ and $\delta = 2$; the antenna used is the helical one. We can notice that the power peaks along a certain line $\omega = \omega(k)$ which roughly represents the real part of the frequency of the quasi-mode. It is easily seen that for each surface the power has a maximum M(r) at definite values of k and ω. Moreover, the plot indicates that for a given equilibrium and fixed values of m, r_a and r_s there exists an optimal resonant surface associated with a maximal power max M(r). This optimal resonant surface can depend on the plasma equilibrium (current j_z, density ρ) or on the antenna structure (azimuthal wave-number m, type of antenna) or geometric factors (position of shell and antennas). By varying these parameters, we try to optimize the Alfvén wave heating.

5.1 Variation of current

The dependence of the maximum of power at a given resonant surface upon the value of j_0 is shown in Fig. 12 for the case where $\alpha = 2$, $\delta = 2$. We notice that for a fixed current profile, the position of the optimal resonant surface is shifted towards the plasma axis when the current increases. At the same time the optimal power is enhanced. Thus, in plasmas with higher β-values we can expect an efficient energy absorption at the innermost surfaces. A peaking of the current profile, the total current being fixed, can have a similar effect. As can be seen from Fig. 13, the optimal resonant surface is shifted towards the plasma axis when the current profile is

steeper. For a very peaked current the energy absorption seems to be equally good for all inner surfaces.

5.2 Variation of density

We first varied the boundary value of the plasma density ρ_a. It turned out that the absorption is not very sensitive to this value. A variation within the range .01 to .1 resulted in a variation of the power by a few per cent. If the density profile is flatter, the optimal resonance surface is shifted towards the plasma surface (up to $r = .63$ if $\delta = 10$); the power is higher but the resonance with the surface quasi-mode is narrower and always occurs near the minimum of ω_A for a given longitudinal wave number k.

5.3 Variation of positions of shell and antennae

By keeping the position of the antenna fixed at $r_a = 1.2$(which is our standard case), we observed an increase of the power, before it saturates, when we increase the position of the outer shell r_s; the Q factor decreases in the same way. This can be seen in Fig. 14 where the resistive absorbed power $\bar{p}$ and the coupling factor Q are plotted versus r_s. If we keep the position of the outer shell fixed at $r_s = 2$ (in all other calculations it was fixed at 1.5) and move the antennae outwards, we observed a decrease of $\bar{p}$ while the Q factor is increasing as demonstrated in Fig. 15. In both cases, the optimal point in the ωk plane is shifted toward lower ω and k. In any case, the resonant behaviour looks the same and the optimal resonant surface remains between .4 and .5.

5.4 Comparison of antennae

The dependence of the maximum of power at a given resonant surface upon the type of antenna used is shown in Fig. 16 for the case m = 1. It appears that the optima of the absorbed power agree within 20 % with each other. In the case of a higher m, however, their ratio increases strongly as shown in Fig. 17; the respective optimal resonant surfaces are shifted towards the plasma boundary and are already around .8 for m = 2. We have still to point out that, in the ωk-plane, the optimum point occurs for lower ω and k when we use the helical antenna. In conclusion, we notice that a good energy absorption by the inner surfaces occurs only in the case m = 1; in this case the results obtained for both antennae are comparable.

5.5 Very-low frequency heating

The Alfvén continuous spectrum can comprise a marginal point where $F = (kB_z + mB_\theta/r) = 0$ and it is then possible to have two resonant layers for low pump frequencies. Such a situation is shown in the lower part of Fig. 18 where the local Alfvén frequency is plotted versus radius. In the upper part we show the coupling parameter W/ξ_r^2 computed by the evolution code, where W is the fractional power deposited at the resonant layers and ξ_r (1) the radial displacement at the edge of the plasma. This factor is calculated separately for the two radial intervals $0 < r < .8$ and $.8 < r < 1$. The results for four different pump frequencies show that the presence of an outer resonant layer does not preclude the inner layer from being heated. Nevertheless, for low frequencies near the marginal point, the

coupling seems bad. This last result is confirmed by the stationary code when we plot, in a logarithmic scale, the power versus the pump frequency (Fig. 19). Furthermore, for low pump frequency ω, the absorbed power decreases as ω^3 as predicted by CANOBBIO (1981). Thus, it does not seem possible to heat the plasma efficiently with very low frequencies. This can be understood if we invoke the foregoing arguments about the collective mode. The applied frequencies are very low, and consequently far from the frequency of the collective mode.

6. MAGNETOSONIC CAVITY MODE COUPLING

Another possibility to couple a global motion to the Alfvén continuum is to excite the second or higher fast magnetosonic waves. In Fig. 20 we present, in a logarithmic scale, the absorbed power $\bar{p}$ versus the pump frequency ω for two different resonant surfaces r_s = .7 and r_s = .5. In this figure, we see different resonant behaviour of the energy deposition: a broad resonance if we couple to the surface quasi-mode, a narrow one if we couple to the second fast magnetosonic wave. The latter result is in qualitative agreement with the previous treatments (OTT et al., 1978; KARNEY et al., 1979; STIX, 1980). Moreover, the more is the resonant surface shifted towards the plasma axis, the greater is the difference between the two coupling schemes. If we look at the amount of energy deposited, the two schemes are equally good for r_s = .7 but differ already by a factor 10^5 for r_s = .5. It appears that for the inner surfaces the optimal case occurs when we couple to the surface quasi-mode. We have made the same study with different density and current profiles and for the coupling to the other fast waves (3rd, 4th, etc.); we have obtained the same qualitative results.

7. CONCLUSION

We have shown that the structure of the antenna and the frequency of the rf generator used for the Alfvén wave excitation can be optimized in such a way that an efficient energy deposition takes place at the innermost plasma surface if we couple to the surface quasi-mode. Also we have shown how this energy deposition depends on density and current profiles as well as on the position of the shell and antenna. We have pointed out that the optimal case occurs for the $m = 1$ excitation; in this case, the results are comparable for both antennae considered. Futhermore, we can conclude that the heating scheme based on the coupling to a strongly-damped surface quasi-mode in the Alfvén continuum looks much more efficient, concerning the position of the resonant surfaces, than the other scheme based on the magnetosonic cavity mode coupling; it is easier to heat the center of the plasma with the first scheme. Nevertheless, a complete description of the Alfvén wave heating would also demand the inclusion of kinetic effects and nonlinearities.

The authors wish to acknowledge the useful discussions with Dr. R. Gruber, Dr. R. Keller, Dr. A. Pochelon and Prof. F. Troyon.

This work was supported by the Ecole Polytechnique Fédérale de Lausanne, by the Swiss National Science Foundation and by Euratom.

REFERENCES

APPERT K., BERGER D., GRUBER R., TROYON F. and ROBERTS K.V. (1975) Comp. Phys. Comm. 10, 11.

CANOBBIO E. (1981) Nucl. Fusion 21, 759.

CHEETHAM A.D., et al. (1980) Centre de Recherches en Physique des Plasmas, Lausanne, Report LRP 162/80.

CHEN L. and HASEGAWA A. (1974) Phys. Fluids 17, 1399.

GROSSMANN W. and TATARONIS J. (1973) Z. Phys. 261, 217.

HASEGAWA A. and CHEN L. (1974) Phys. Rev. Lett. 32, 454.

KARNEY C.F.F., PERKINS F.W. and SUN Y.C. (1979) Phys. Rev. Letters 42, 1621.

OTT E., WERSINGER J.M. and BONOLI P.T. (1978) Phys. Fluids 21, 2306.

SEDLACEK Z. (1971) J. Plasma Phys. 5, 239.

STIX T.H. (1980) 2nd Joint Varenna-Grenoble International Symposium on Heating in Toroidal Plasmas, 3-12 september, Como.

FIGURE CAPTIONS

Fig. 1 Schematic diagram of the plasma-antenna-shell configuration.

Fig. 2 Schematic diagram of the helical antenna.

Fig. 3 Schematic diagram of the TCA antenna.

Fig. 4 Time evolution of poloidal displacement and absorbed power.

Fig. 5 Stationary response of poloidal displacement and absorbed power for different artificial damping rates versus radius.

Fig. 6 Density profile used to demonstrate a plasma global motion.

Fig. 7 Fourier amplitudes of the radial displacement at three different radii.

Fig. 8 Collective mode resonance of the absorbed power.

Fig. 9 Absorbed power versus time.

Fig. 10 Absorbed power versus artificial damping rate.

Fig. 11 Altitude chart of the absorbed power for $m = 1$, $j_0 = .6$, $\alpha = 2$ and $\delta = 2$.

Fig. 12 Maximal absorbed power versus the position of resonant surface for different equilibrium currents of the same profile. The parameters used are: $m = 1$, $\alpha = 2$ and $\delta = 2$.

Fig. 13 Maximal absorbed power versus the position of resonant surface for different profiles of the same equilibrium current. The parameters used are: $m = 1$ and $\alpha = 2$.

Fig. 14 Absorbed power and the coupling factor versus the position of the shell.

Fig. 15 Absorbed power and the coupling factor versus the position of the antenna.

Fig. 16 Maximal absorbed power versus the position of resonant surface for two different antennae; $m = 1$.

Fig. 17 Ratio of maximal absorbed power and the position of the optimal resonant surface for two different antennae versus m.

Fig. 18 The coupling parameter W/ξ_r^2 and the Alfvén frequency ω_A versus radius in the case of two resonant surfaces. The parameters used are: $m = -2$, $k = 3$, $j_0 = .6$, $\alpha = 2$ and $\delta = 2$.

Fig. 19 Absorbed power versus the pump frequency for $k = .3$ (Δ) and $k = .5$ (O). The other parameters used are: $m = -2$, $j_0 = .6$, $\alpha = 2$ and $\delta = 2$.

Fig. 20 Absorbed power versus the pump frequency for two different resonant surfaces. The parameters used are: $m = 1$, $j_0 = .6$, $\alpha = 2$ and $\delta = 2$.

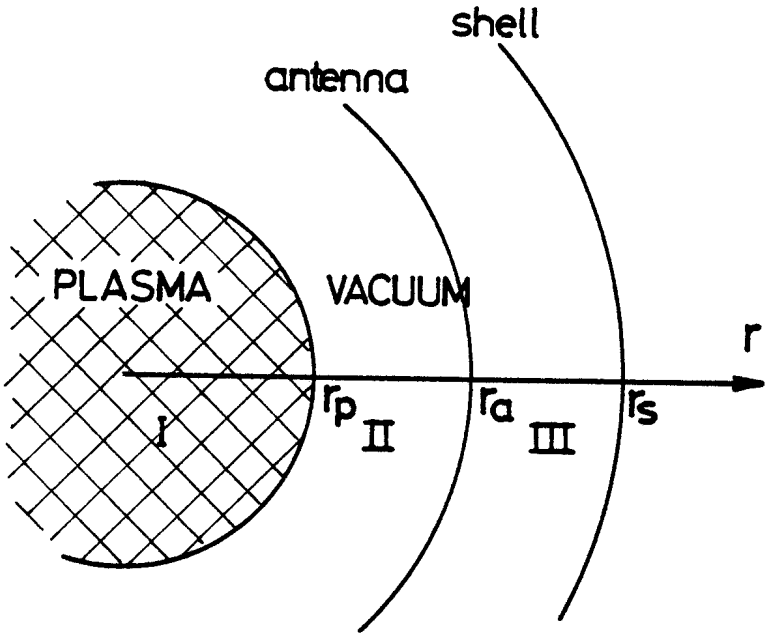

Fig. 1

HELICAL ANTENNA

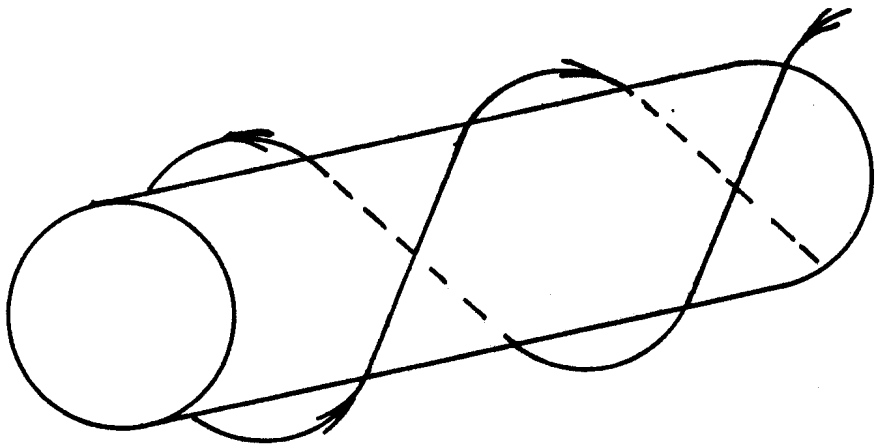

Fig. 2

TCA ANTENNA

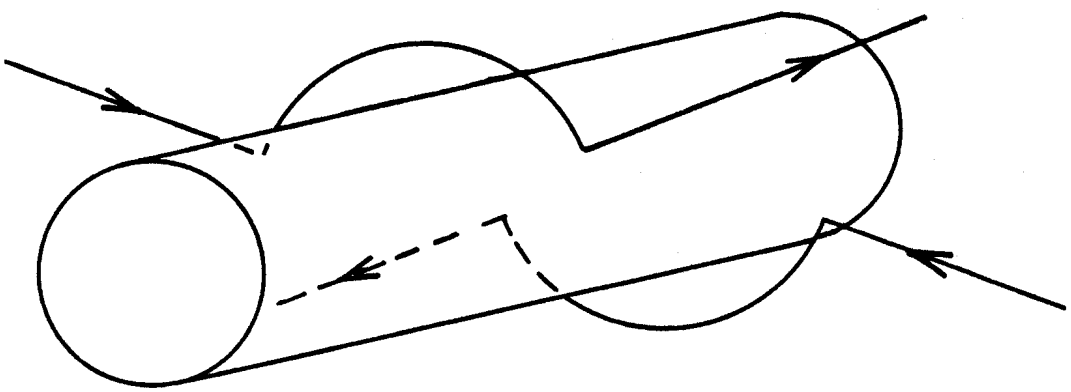

Fig. 3

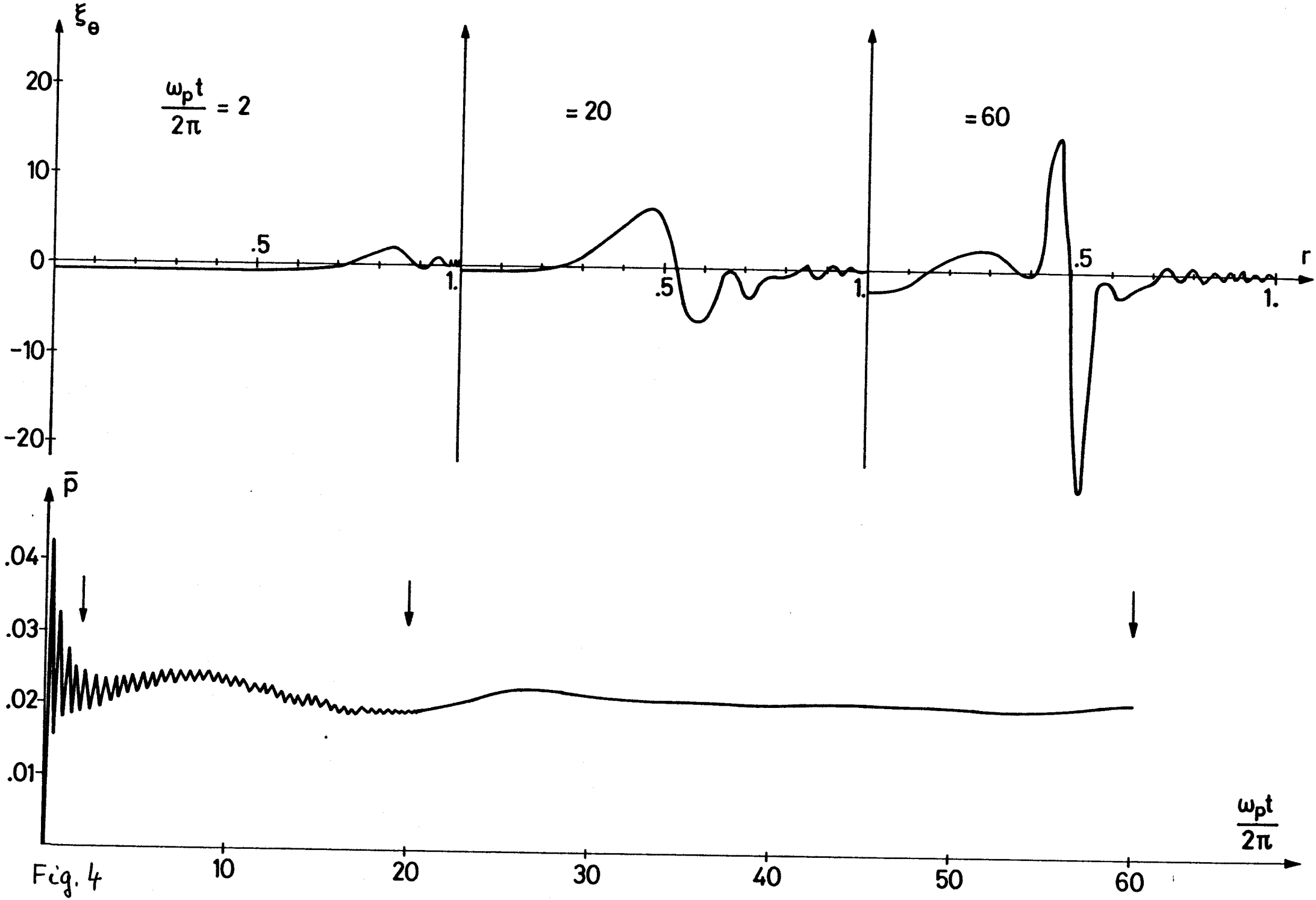
ξ_θ
20
10
0
-10
-20
$\frac{\omega_p t}{2\pi} = 2$
= 20
= 60
.5
1.
.5
1.
.5
1.
r
$\bar{p}$
.04
.03
.02
.01
10
20
30
40
50
60
$\frac{\omega_p t}{2\pi}$

Fig. 4

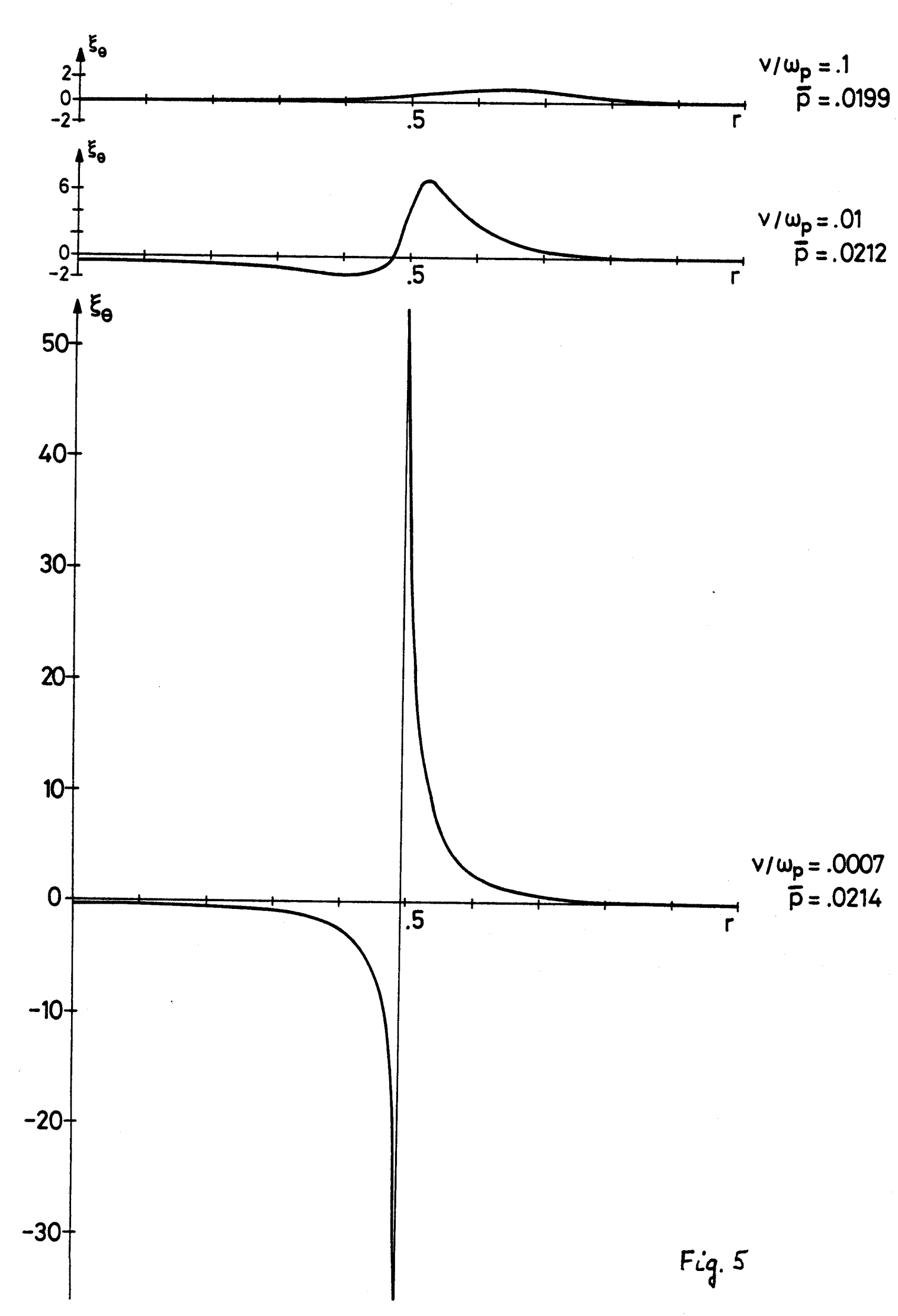
ξ_θ
2
0
-2
.5
r
$\nu/\omega_p = .1$
$\bar{p} = .0199$
ξ_θ
6
0
-2
.5
r
$\nu/\omega_p = .01$
$\bar{p} = .0212$
ξ_θ
50
40
30
20
10
0
-10
-20
-30
.5
r
$\nu/\omega_p = .0007$
$\bar{p} = .0214$

Fig. 5

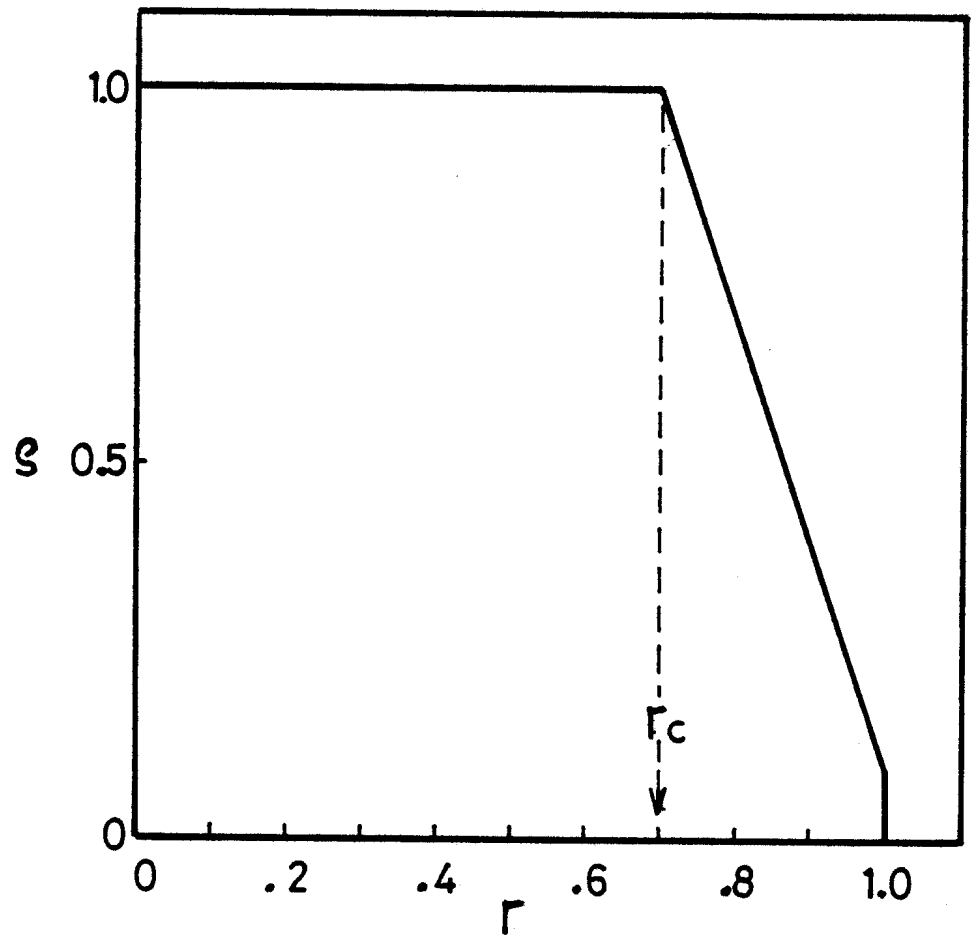

Fig. 6

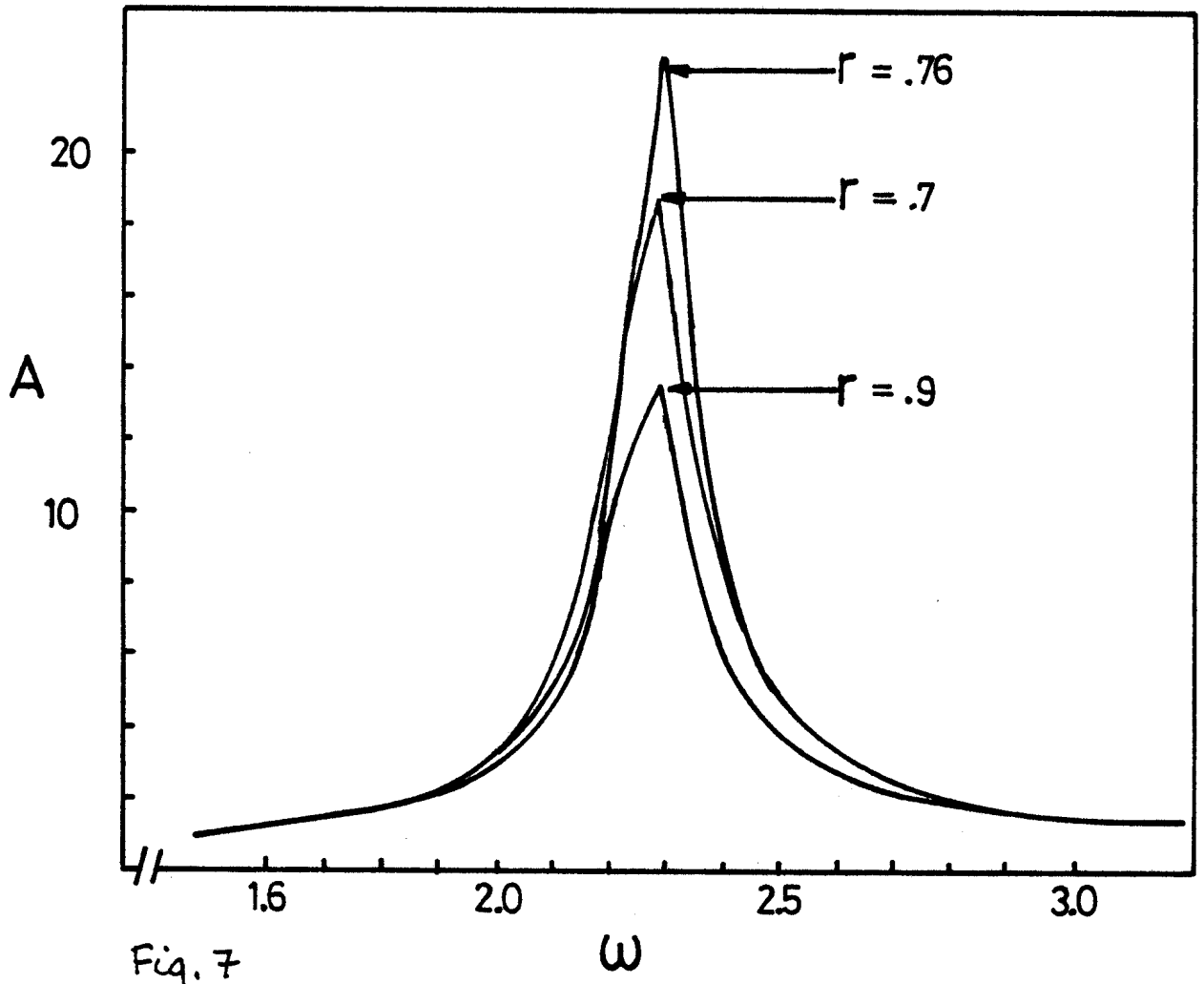

Fig. 7

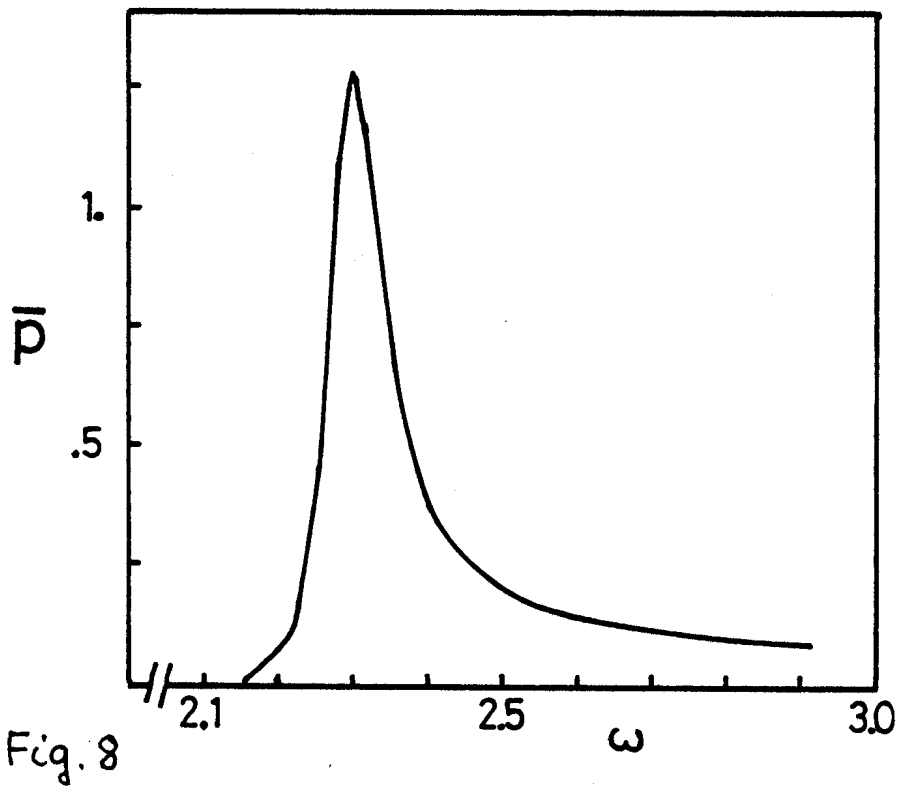

Fig. 8

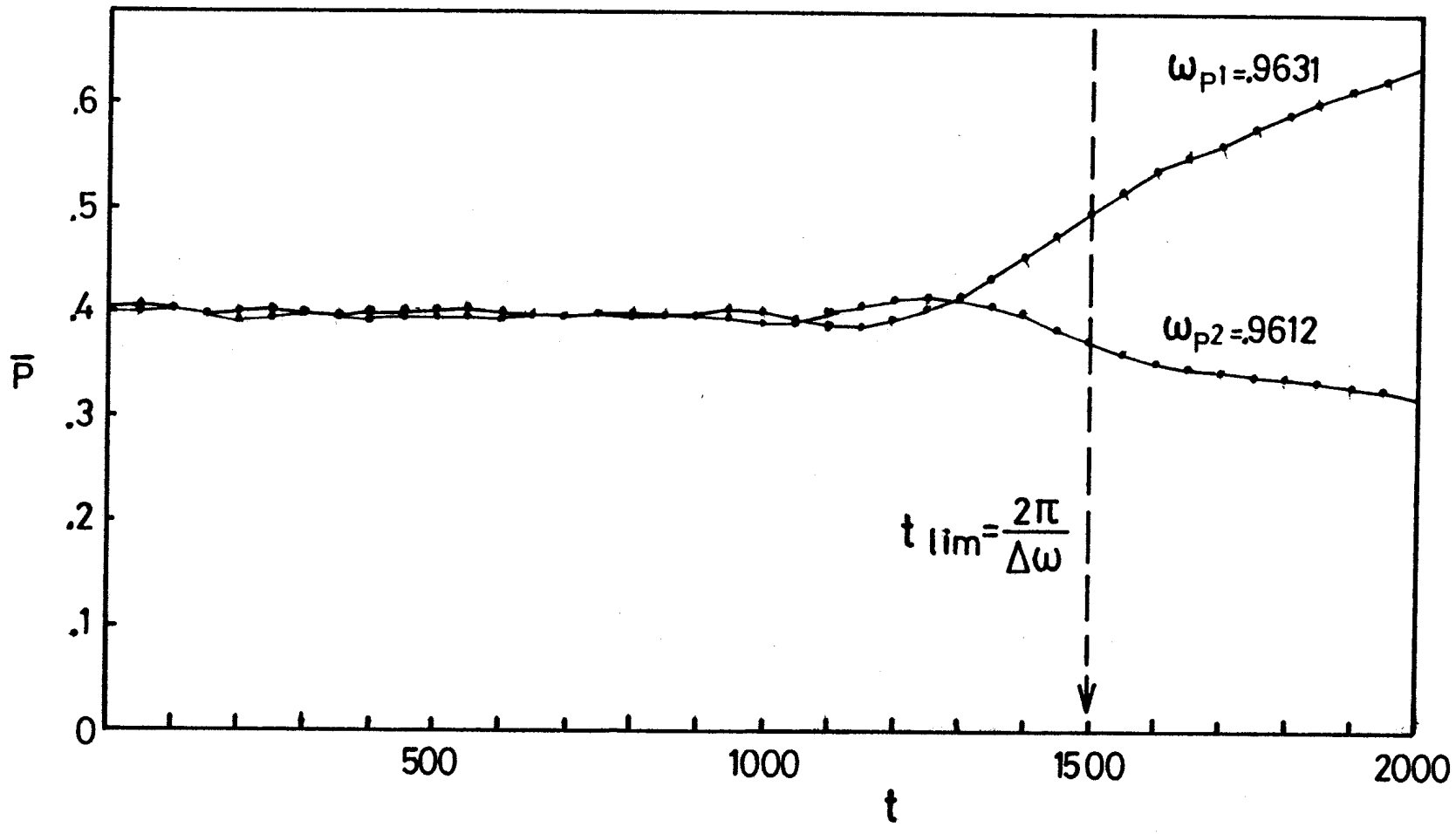
ω_{p1}=.9631
ω_{p2}=.9612
$t_{lim}=\frac{2\pi}{\Delta\omega}$
$\bar{P}$
.6
.5
.4
.3
.2
.1
0
500
1000
1500
2000
t

Fig. 9

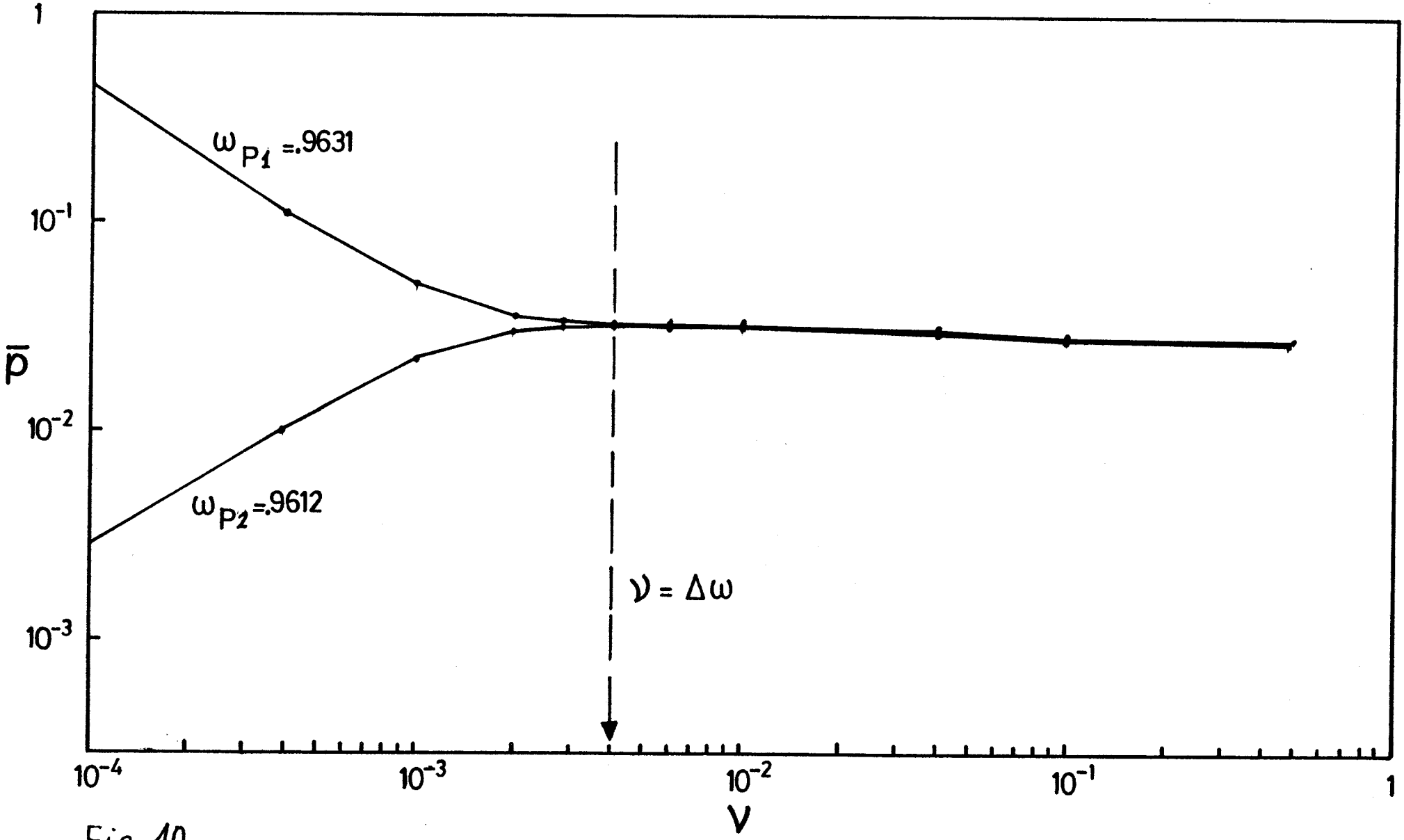
1
10^{-1}
10^{-2}
10^{-3}
$\bar{p}$
ω_{P1} =.9631
ω_{P2}=.9612
$\nu = \Delta\omega$
10^{-4}
10^{-3}
10^{-2}
10^{-1}
1
ν

Fig. 10

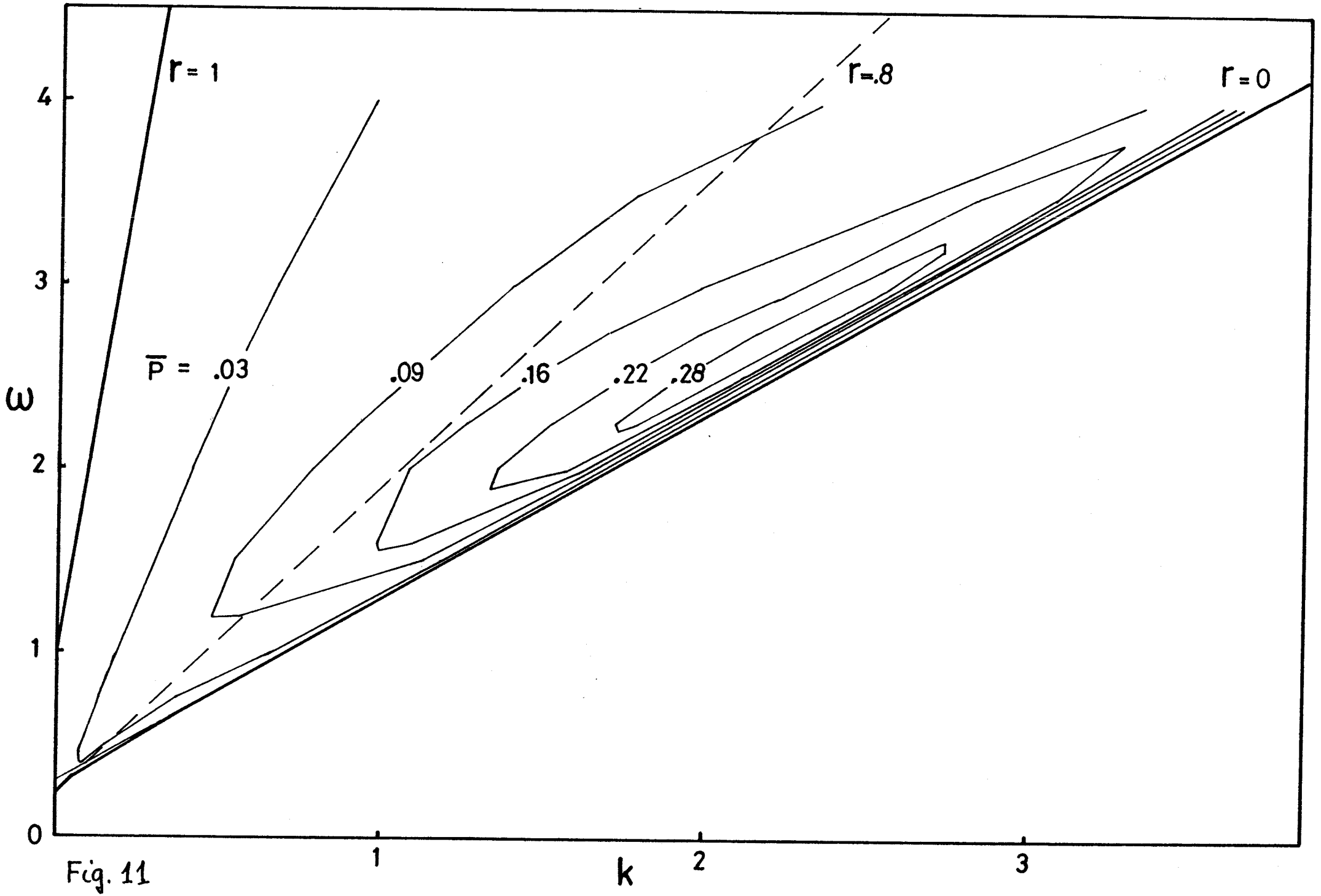

Fig. 11

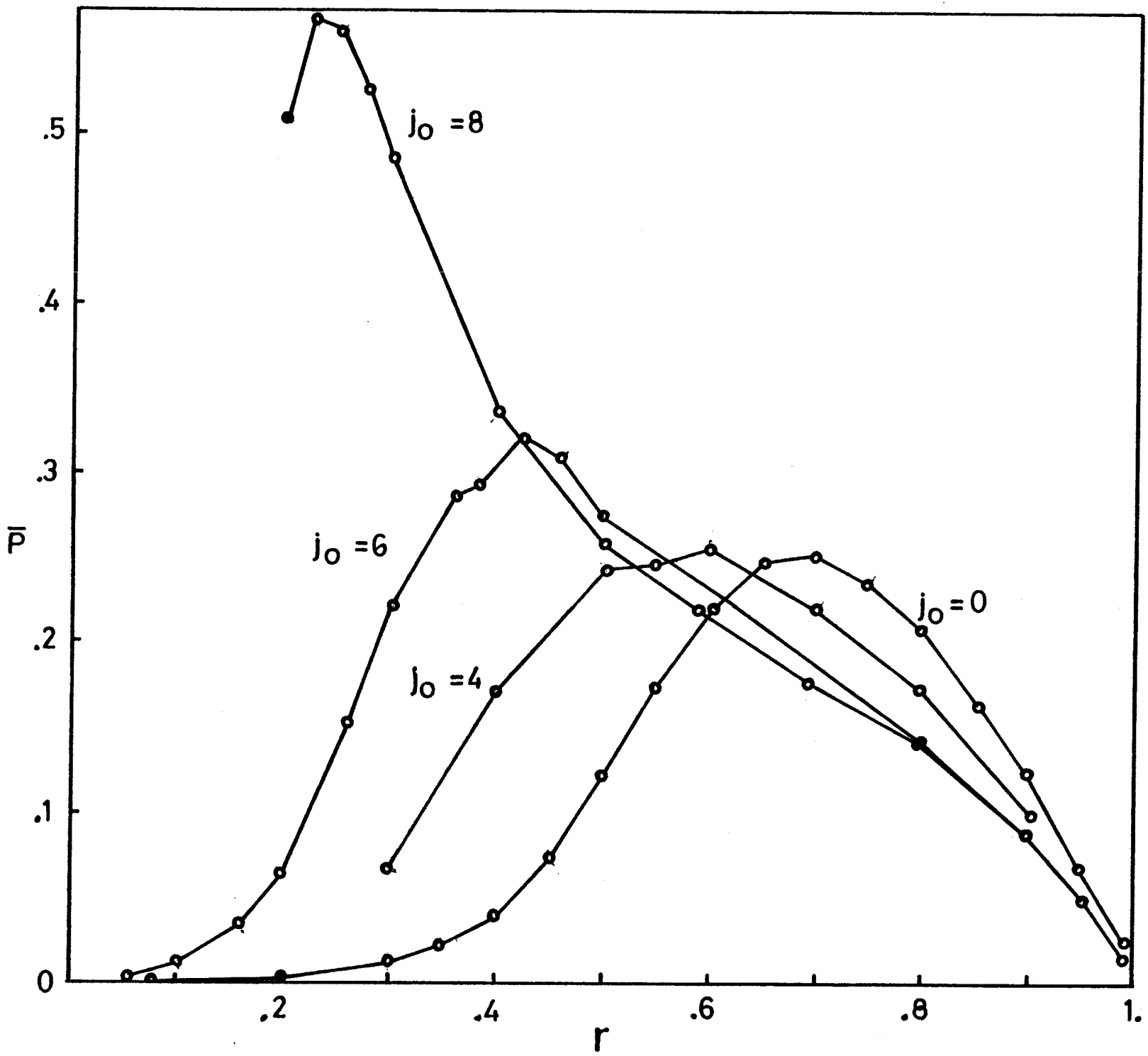

Fig. 12

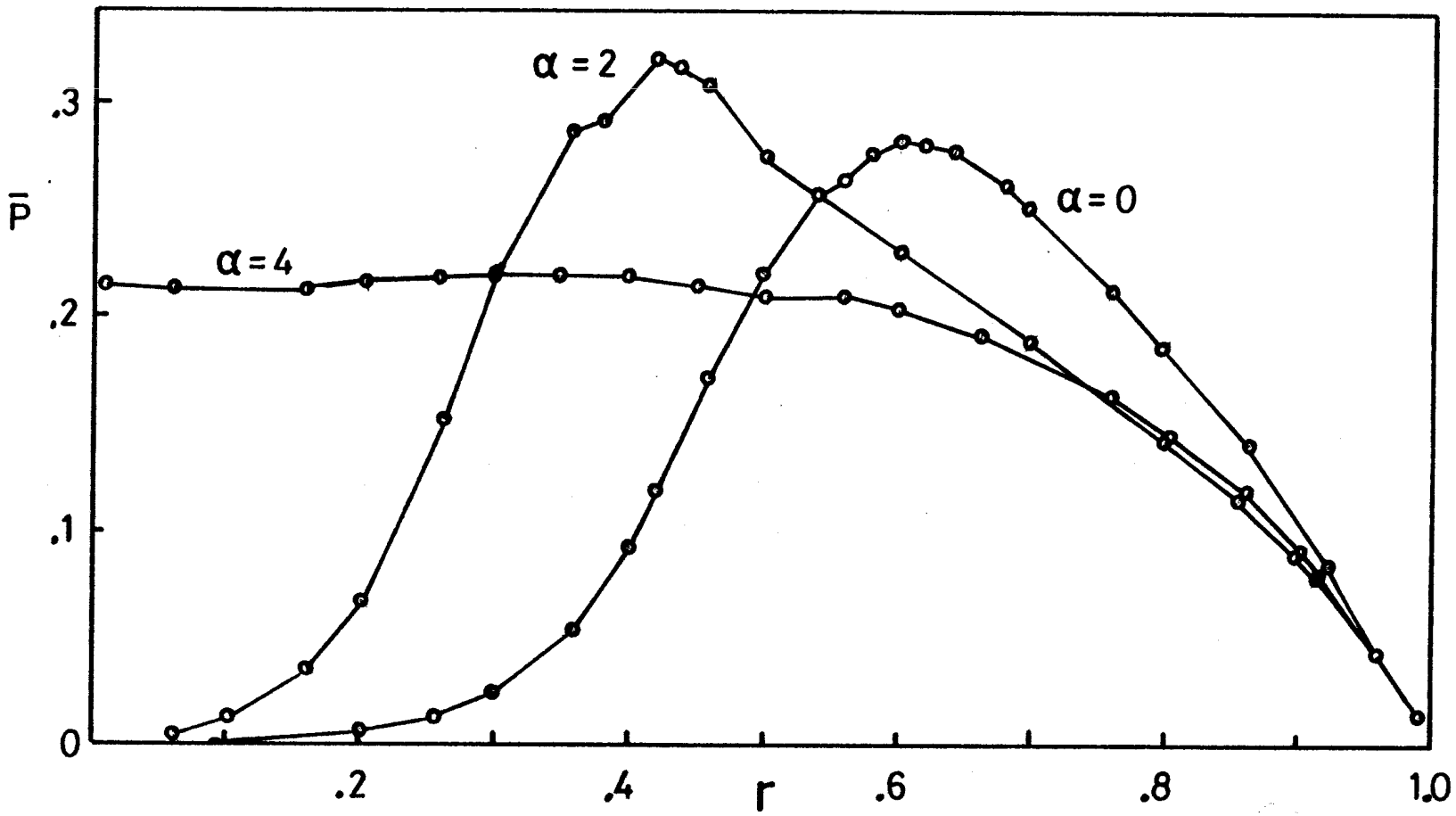

Fig. 13

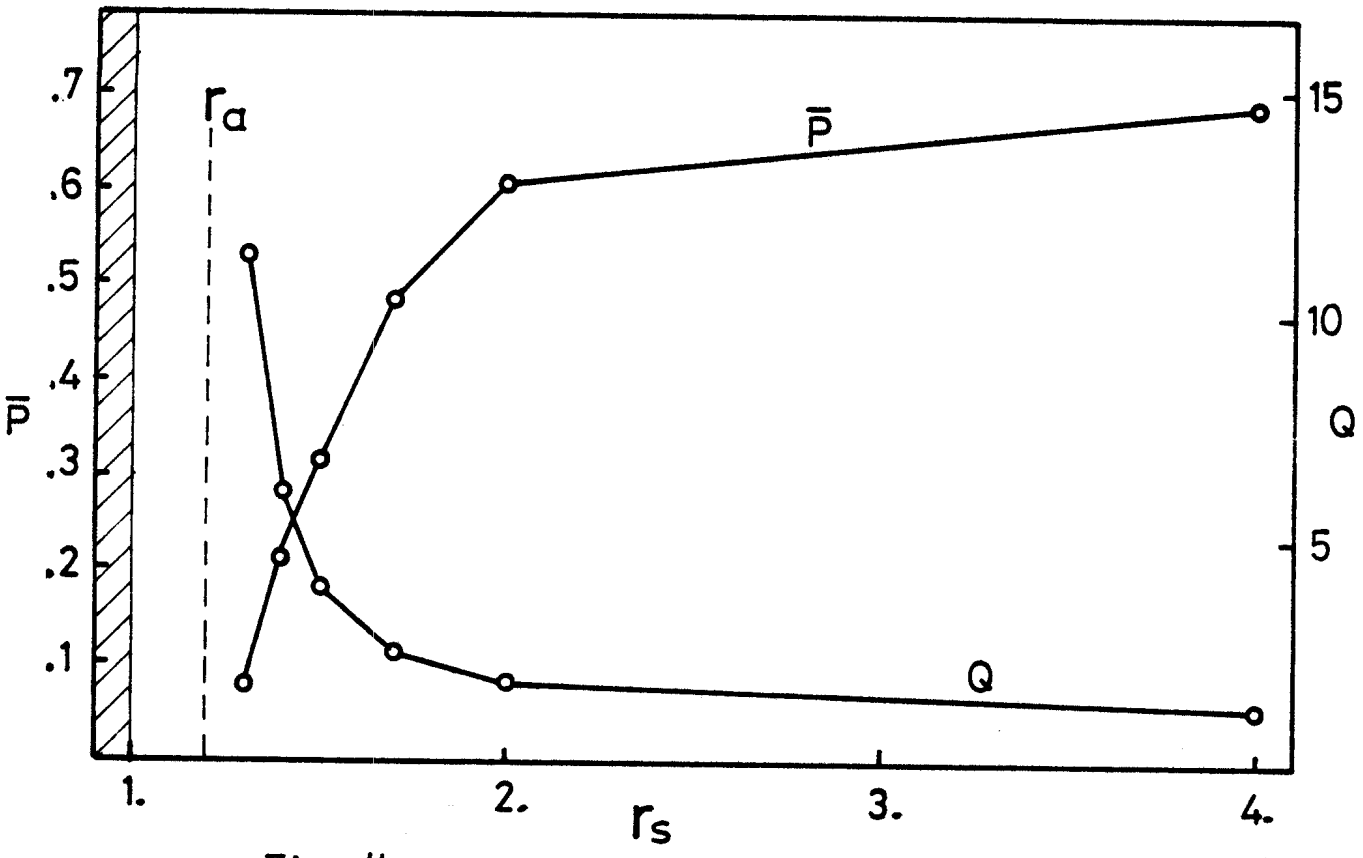
.7
.6
.5
.4
.3
.2
.1
$\bar{P}$
r_a
$\bar{P}$
Q
15
10
5
Q
1.
2.
3.
4.
r_s

Fig. 14

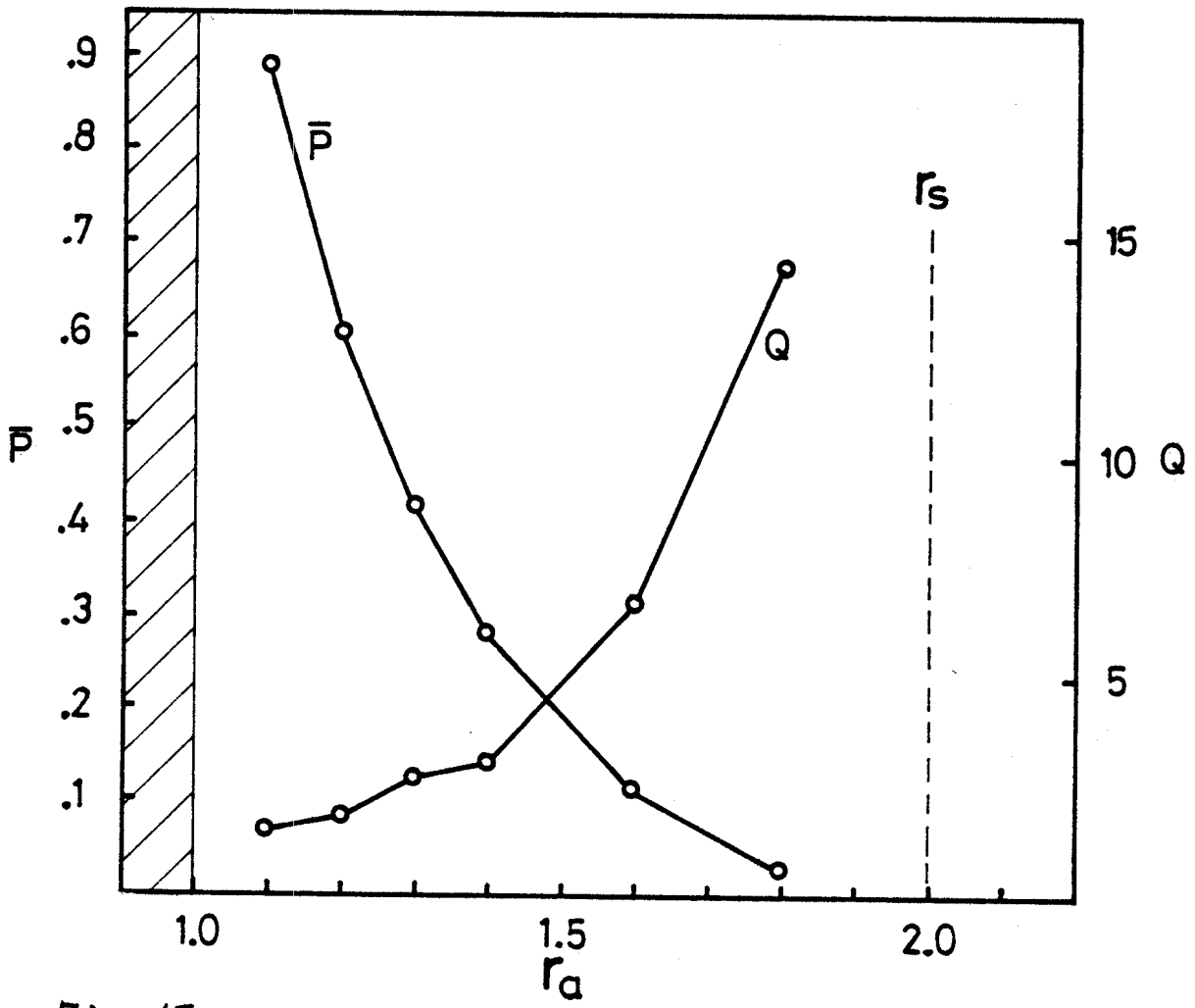
.9
.8
.7
.6
.5
.4
.3
.2
.1
$\bar{P}$
$\bar{P}$
r_s
Q
15
10 Q
5
1.0
1.5
2.0
r_a

Fig. 15

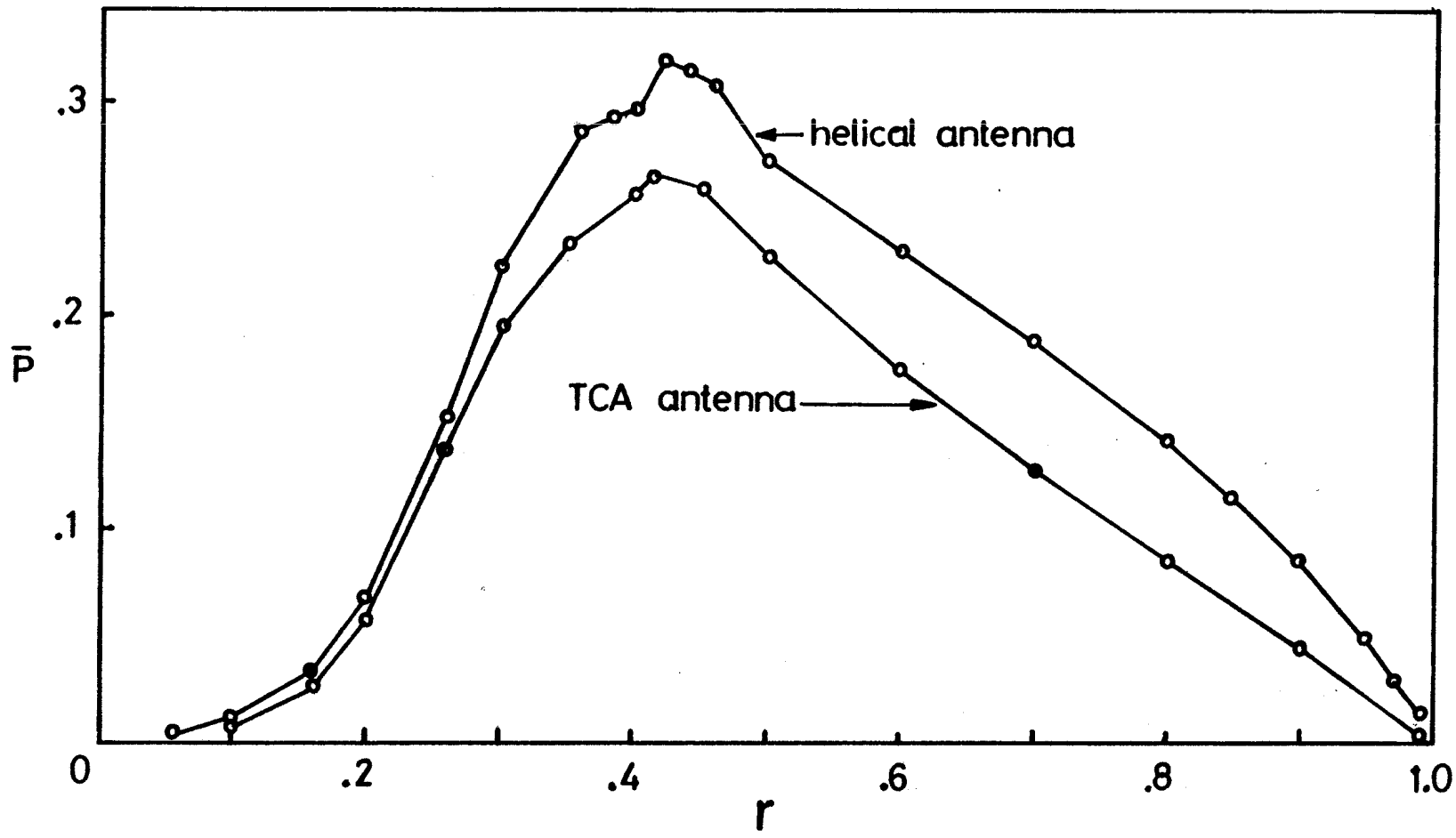

Fig. 16

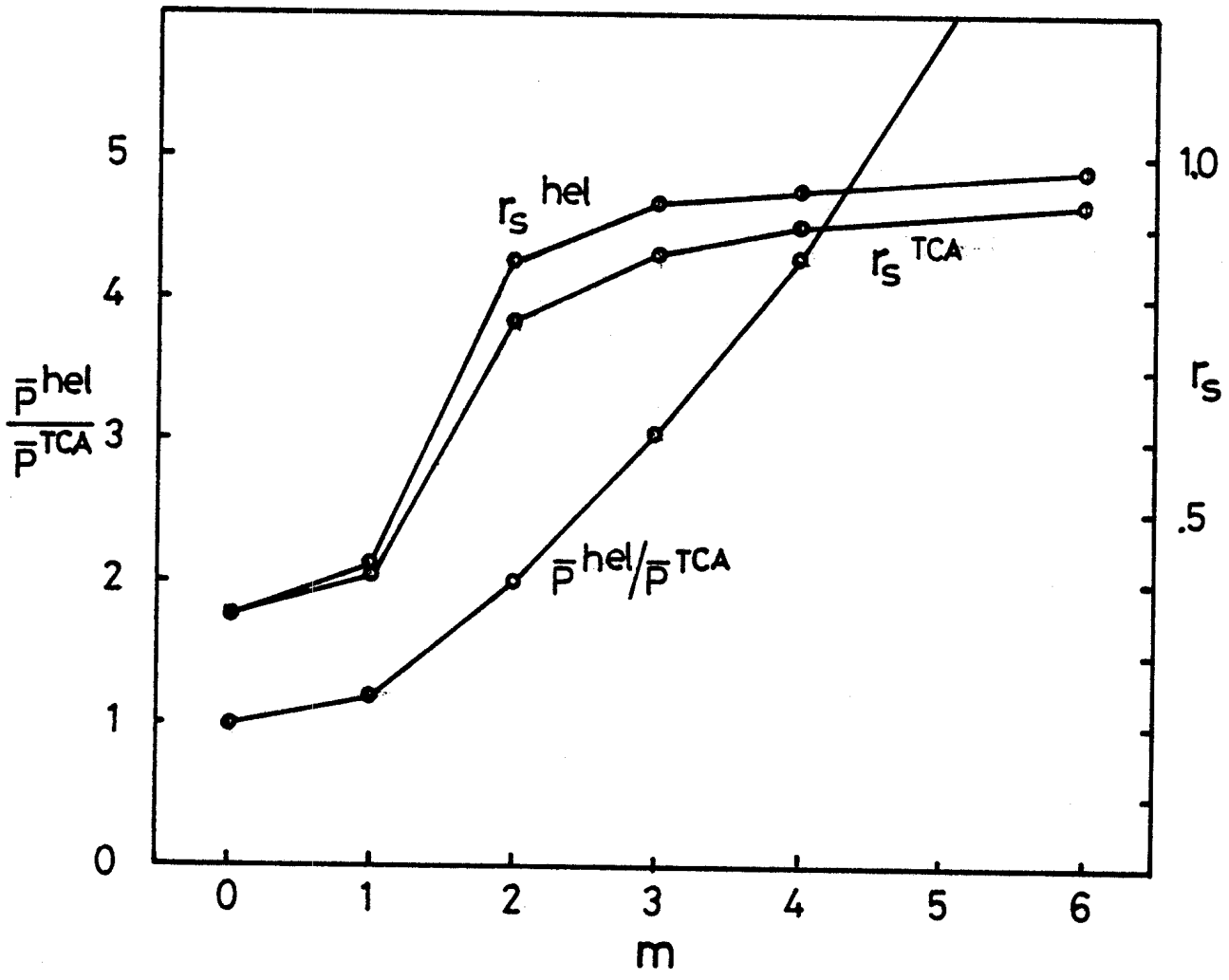
5
4
3
2
1
0
$\frac{\bar{P}^{hel}}{\bar{P}^{TCA}}$
0
1
2
3
4
5
6
m
1.0
.5
r_s
r_s^{hel}
r_s^{TCA}
$\bar{P}^{hel}/\bar{P}^{TCA}$

Fig. 17

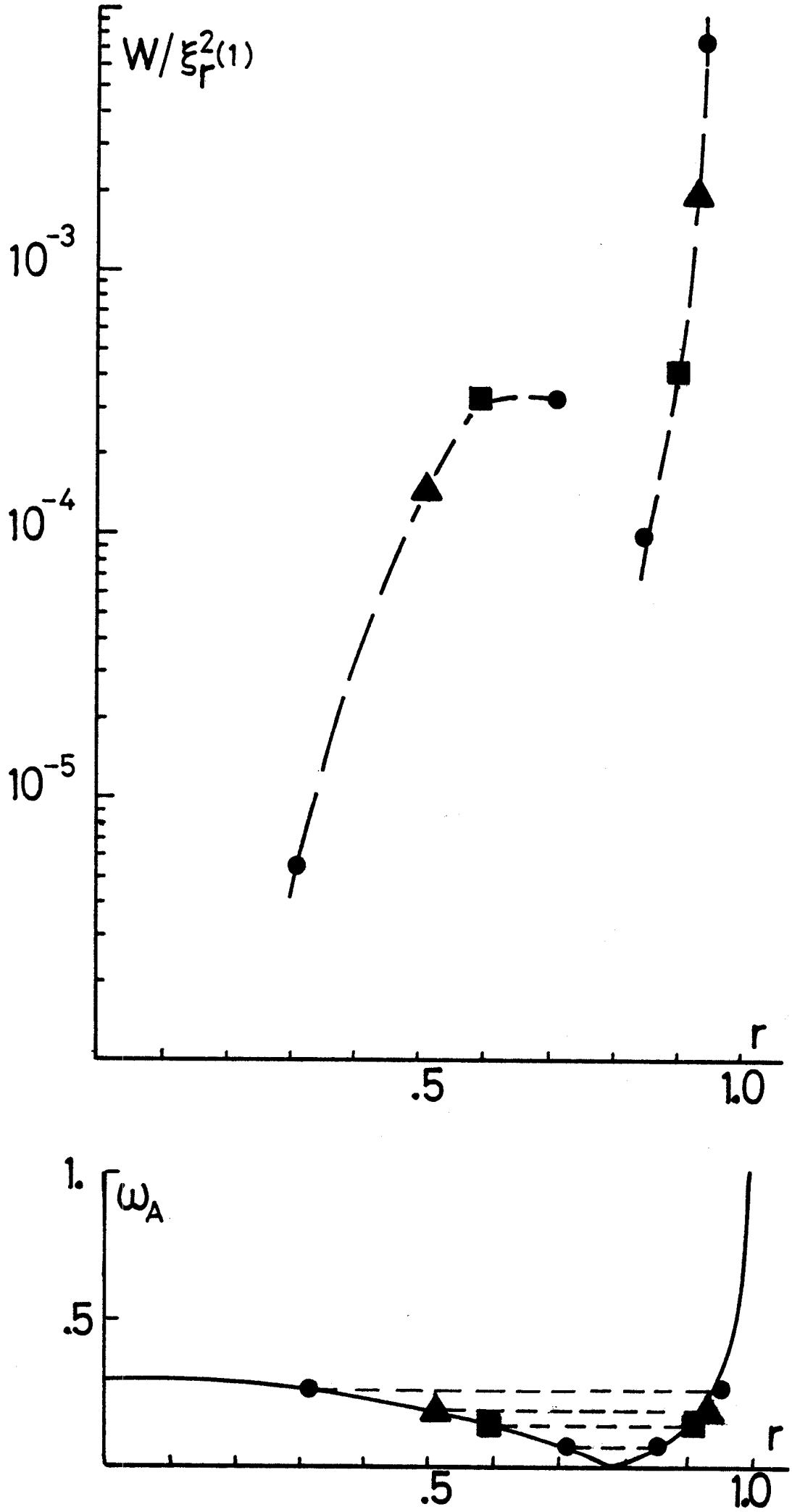

Fig. 18

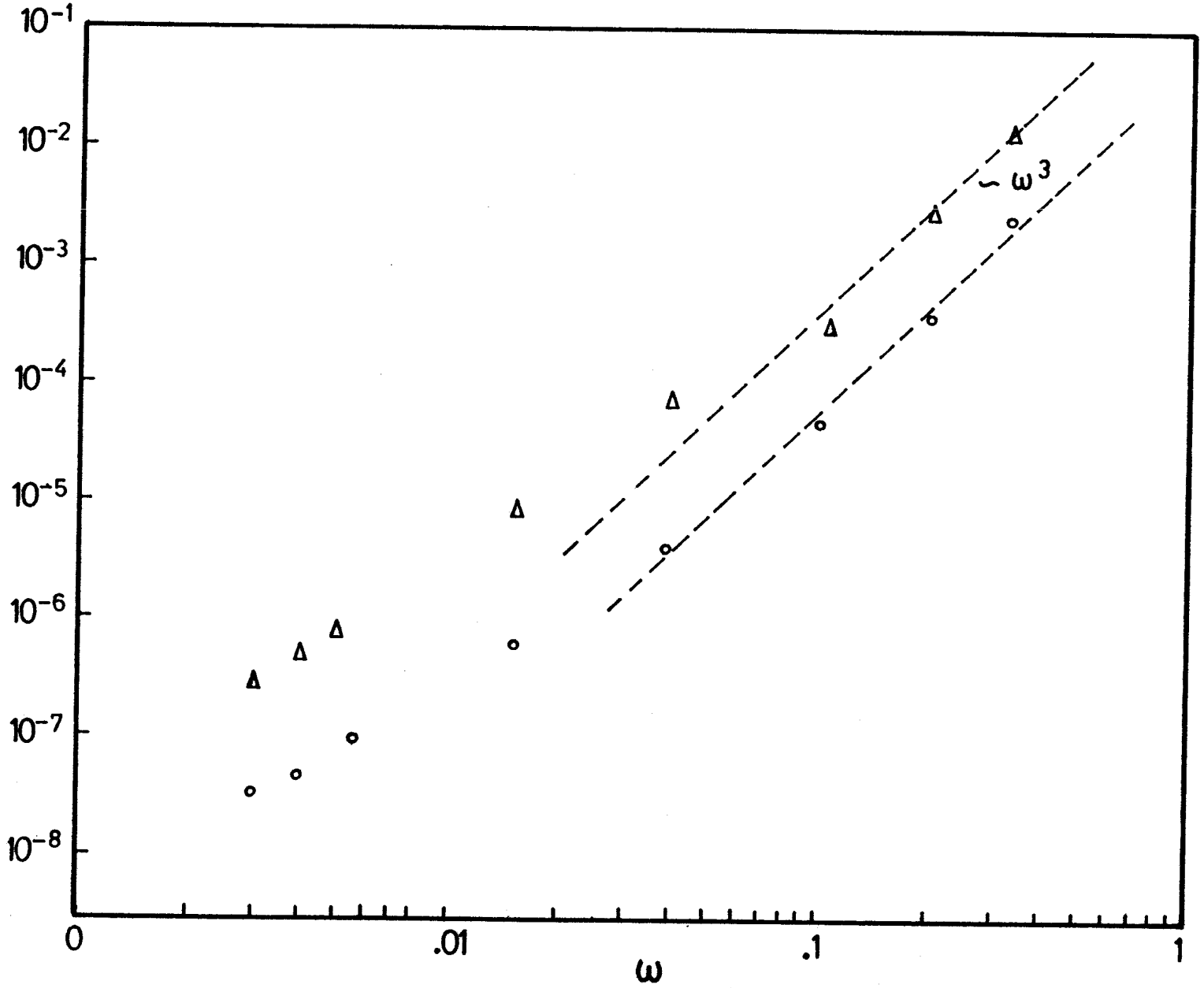

Fig. 19

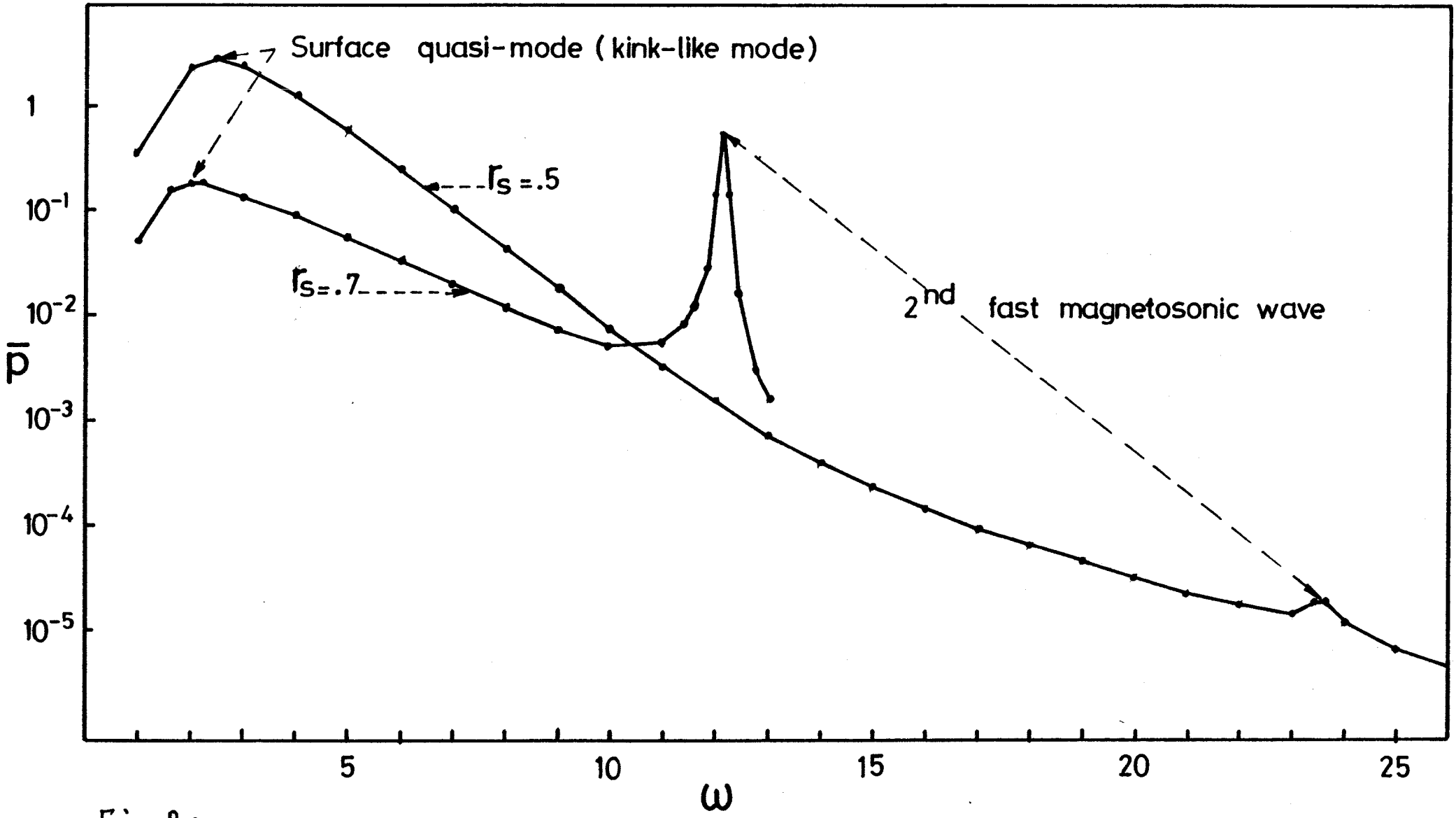
Surface quasi-mode (kink-like mode)
$r_s = .5$
$r_s = .7$
2nd fast magnetosonic wave
1
10^{-1}
10^{-2}
10^{-3}
10^{-4}
10^{-5}
$\bar{p}$
5
10
15
20
25
ω

Fig. 20